

Evaluating the Model Representation of Asian Summer Monsoon UTLS Transport and Composition using Airborne In Situ Observations

Warren P. Smith¹, Laura L. Pan¹, Douglas Kinnison¹, Elliot Atlas², Shawn Honomichl¹, Jun Zhang¹, Simone Tilmes¹, Rafael P. Fernandez³, Alfonso Saiz-Lopez⁴, Victoria Treadaway^{5,6}, Karina E. Adcock⁷, Johannes C. Laube⁸, Marc von Hobe⁸, Corinna Kloss⁸, Silvia Viciani⁹, Francesco D'Amato⁹, C. Michael Volk¹⁰, Fabrizio Ravegnani¹¹

¹Atmospheric Chemistry Observations & Modeling Laboratory, National Center for Atmospheric Research, Boulder, Colorado, USA

²Department of Atmospheric Sciences, Rosenstiel School of Marine, Atmospheric, and Earth Science, University of Miami, Miami, Florida, USA

³Institute for Interdisciplinary Science (ICB), National Research Council (CONICET), FCEN-UNCuyo, Mendoza, Argentina

⁴Department of Atmospheric Chemistry and Climate, Institute of Physical Chemistry Blas Cabrera, CSIC, Madrid, Spain

⁵Cooperative Institute for Research in Environmental Sciences, University of Colorado Boulder, Boulder, Colorado, USA

⁶NOAA Chemical Sciences Laboratory, Boulder, Colorado USA

⁷Centre for Ocean and Atmospheric Sciences, School of Environmental Sciences, University of East Anglia, Norwich, UK

⁸Institute for Energy and Climate Research (IEK-7), Forschungszentrum Jülich GmbH, 52425 Jülich, Germany

⁹National Research Council - National Institute of Optics (CNR-INO), Sesto Fiorentino, Italy

¹⁰University of Wuppertal, Germany

¹¹Institute of Atmospheric Sciences and Climate, Bologna, Italy

Key Points:

- We develop process-based diagnostics for model evaluation using airborne in situ observations
- We analyze the representation of the Asian summer monsoon for its role in impacting composition and climate
- The established diagnostics use dynamical and chemical coordinates to identify areas for model improvement

Corresponding author: Warren P. Smith, wsmith@ucar.edu

Abstract

Chemistry transport models (CTMs) are essential tools for characterizing and predicting the role of atmospheric composition and chemistry in Earth's climate system. This study demonstrates the use of airborne in situ observations to diagnose the representation of atmospheric composition by global CTMs. Process-based diagnostics are developed which minimize the spatial and temporal sampling differences between airborne in situ measurements and CTM grid points. The developed diagnostics make use of dynamical and chemical vertical coordinates as a means of highlighting areas where focused model improvement is needed. The chosen process is the chemical impact of the Asian summer monsoon (ASM), where deep convection serves a unique pathway for rapid transport of surface emissions and pollutants to the stratosphere. Two global CTM configurations are examined for their representation of the ASM upper troposphere and lower stratosphere (UTLS), using airborne observations collected over south Asia. Application of the developed diagnostics to the CTMs reveals the limitations of zonally-averaged surface boundary conditions for species with sufficiently short tropospheric lifetimes, and that species whose stratospheric loss rates are dominated by photolysis have excellent agreement compared to that observed. Overall, the diagnostics demonstrate the strength of airborne observations toward improving model predictions, and highlight the utility of high-resolution climate modeling to improve the understanding of reactive transport of anthropogenic pollutants to the stratosphere.

Plain Language Summary

The chemical composition of Earth's atmosphere has important implications for the health of all its ecosystems. This study establishes an approach for evaluating the representation of chemical composition in global climate models, and demonstrates the capabilities of the approach using a set of observations collected by research aircraft. We specifically focus the evaluation on the Asian summer monsoon, a region with a known pathway for transport of chemical species from near the surface into the upper atmosphere. In doing so, we identify specific areas where focused model improvement is needed.

1 Introduction

The chemical composition of Earth's atmosphere has implications for its climate and the health of all its ecosystems. Changes in atmospheric composition, induced by changes in both natural processes and anthropogenic activities, may have impacts on surface air quality, the atmosphere's energy budget, the delay of stratospheric ozone recovery as set in motion by the Montreal Protocol, among others. As such, ensuring the accurate characterization and prediction of past, present and future atmospheric composition remains a compelling research avenue.

Chemistry-climate models (CCMs) are commonly used tools to characterize and predict atmospheric composition. This type of model often sacrifices horizontal grid spacing (typically tens to hundreds of kilometers) in favor of simulating extended time periods (years to decades) with global coverage (e.g., Danabasoglu et al., 2020). Trust in any model to accurately predict the future fundamentally hinges upon its adequate representation of the past and present. Often CCMs are evaluated with satellite products and monitoring station observations using time- (e.g., monthly) or spatially- (e.g., zonal average or prescribed regions) averaged comparisons (e.g., Gettelman et al., 2019; Bosso lasco et al., 2021; Strahan et al., 2007; Froidevaux et al., 2019). Despite the known impact of regional-scale processes on atmospheric composition and climate, these processes must typically be parameterized in CCMs because their spatial (on the order of kilometers) and temporal (on the order of hours) scales are not compatible with a typical CCM's grid configuration. To evaluate and improve the representation of regional-scale processes

83 in CCMs, it is necessary to evaluate them for shorter time periods or for specific regions.
84 In this configuration, a CCM is integrated as a chemistry transport model (CTM).

85 Airborne field campaigns for targeted regions and/or specific phenomena can provide
86 observations to elucidate regional-scale processes affecting atmospheric composition
87 (e.g., Pan et al., 2010, 2017; Toon et al., 2016). Airborne instruments have the capability
88 to sample a portion of the atmosphere in unparalleled detail given their high sampling
89 frequency. However, the high spatial and temporal resolution over a confined area
90 fall into sharp contrast with the grid structures of CTMs, which can make their application
91 for model evaluation difficult to reconcile. Global CTMs typically use horizontal
92 grid spacing of tens or hundreds of kilometers, making them much coarser than airborne
93 in situ observations which are often spaced at hundreds or thousands of meters.
94 As such, specific diagnostic tools are needed to minimize the fundamental differences in
95 air mass sizes represented by in situ observations and CTMs. A straightforward technique
96 is to interpolate a flight track onto a CTM’s grid and compare this with observations
97 taken along the same flight track, but given the aforementioned disparities in air
98 mass sizes this approach may underutilize the full capabilities of both the observations
99 and model.

100 The goal of this study is to demonstrate the use of airborne in situ observations
101 to diagnose CTM representation of deep convective transport to the UTLS and subsequent
102 stratospheric loss processes. Specifically, we present newly-developed process-based
103 diagnostics which use both dynamical and chemical coordinates to minimize the fundamental
104 differences in air mass sizes represented by airborne in situ observations and CTMs.
105 Surface boundary conditions (i.e., surface mixing ratios), dynamics, and chemistry are
106 all considered in the diagnostic development. In doing so, we demonstrate the wealth
107 of information contained within airborne in situ observations, and show that this approach
108 of connecting observations and models enhances the value of each.

109 The specific process of the present evaluation is the Asian summer monsoon (ASM),
110 a dominant weather system during boreal summer which has long been known for its generation
111 of seasonal rainfall over portions of Asia (e.g., Yin, 1949). The line of research
112 we focus on in this work concerns the air mass that is transported from the Asian boundary
113 layer (BL) through ASM deep convection and its subsequent transport. Specifically,
114 water vapor and tropospheric pollutants can be transported vertically through convection
115 to reach the upper troposphere and lower stratosphere (UTLS), where they have
116 the potential to impact global atmospheric composition and climate (e.g., Dethof et al.,
117 1999; Fu et al., 2006; Chen et al., 2012; Fan et al., 2017). The application of chemical
118 and transport modeling techniques to predict ASM impacts on global atmospheric composition
119 remains an active research area (e.g., Ploeger et al., 2017; Vogel et al., 2019; Yan
120 et al., 2019; Pan et al., 2016, 2022; Clemens et al., 2023).

121 The dynamical response to ASM deep convection, an anticyclone which forms in
122 the UTLS during boreal summer (Krishnamurti & Bhalme, 1976), has been observed by
123 satellite to show confinement of anomalous pollutant concentrations of anthropogenic
124 signature (e.g., Park et al., 2004, 2007; Randel et al., 2010). Tropopause altitudes over
125 the ASM are typically higher than the surrounding regions, so ASM pollutants detrained
126 from deep convection may be subsequently transported to the stratosphere through quasi-
127 isentropic mixing as they spiral upward anticyclonically (e.g., Pan et al., 2016; Vogel et
128 al., 2019; Legras & Bucci, 2020). Short-lived halogenated species transported to the UTLS
129 in this way may delay the recovery of stratospheric ozone (e.g., Bednarz et al., 2022),
130 where the modeled impact depends on the complexity of the chemical mechanism or treatment
131 considered (Fernandez et al., 2021). The potential for the ASM to impact atmospheric
132 composition and climate makes it an ideal setting for the development of CTM
133 evaluation diagnostics.

Table 1. A collection of StratoClim data used for the development of model diagnostics in this study, including the sensors or instruments that obtained them.

Instrument	Species Used	PI	Reference
AMICA	Carbon Monoxide (CO)	M. von Hobe	Kloss et al. (2021)
COLD2	Carbon Monoxide (CO)	S. Viciani	Viciani et al. (2018)
FOZAN-II	Ozone (O ₃)	F. Ravagnani	Ulanovsky et al. (2001)
HAGAR	Nitrous Oxide (N ₂ O)	C. M. Volk	Homan et al. (2010)
WAS	Halogenated Species	J. Laube	Adcock et al. (2021)

134 The model evaluation and diagnostic development is broken down into three spe-
135 cific processes which loosely encompass the pathway for anthropogenic pollution emit-
136 ted over Asia to impact UTLS composition, and thus global climate. Each analyzed pro-
137 cess results in the development of a diagnostic, and is presented in its own subsection
138 within Section 3. First, we use an adjusted-tropopause relative altitude coordinate to
139 diagnose transport of polluted air masses from the Asian BL to the ASM UTLS anti-
140 cyclone via deep convection (Section 3.1). Next, we diagnose the modeled mixing ratios
141 of halogenated species as they cross the ASM tropopause and enter the stratosphere (Sec-
142 tion 3.2). Finally, we diagnose model chemical loss rates in the stratosphere by using the
143 mixing ratio of long-lived tracers as a vertical coordinate (Section 3.3). To demonstrate
144 the value of the diagnostic development, we evaluate two CTMs with different grid con-
145 figurations (Section 2.2) by using a set of airborne in situ observations taken over south
146 Asia during the ASM’s active period (Section 2.1).

147 2 Tools for Diagnostic Development

148 2.1 Airborne in situ observations from StratoClim 2017

149 Motivated by the pronounced impacts of the ASM on UTLS composition, the Stra-
150 toClim airborne field campaign (<http://www.stratoclim.org/>; von Hobe et al., 2021; Bucci
151 et al., 2020) was conducted during boreal summers 2016 and 2017 with bases in Kala-
152 mata, Greece and Kathmandu, Nepal, respectively. As the 2017 deployment took place
153 over southern Asia, the region identified as the predominant source of convective uplift
154 for the ASM UTLS anticyclone (e.g., Bergman et al., 2013; Vogel et al., 2015; Pan et al.,
155 2016), we use only the 2017 observations throughout this paper, and henceforth refer to
156 this deployment as “the StratoClim campaign” for simplicity. The StratoClim campaign
157 conducted eight research flights onboard the M55 Geophysica between July 27 and Au-
158 gust 10, 2017. The location of the experiment is shown in Figure 1 with dynamical con-
159 text. The research flights primarily sampled the interior of the ASM UTLS anticyclone
160 (e.g., Figure 1 of von Hobe et al., 2021). Here we also show the flight tracks relative to
161 the seasonal location of the anticyclone from a geopotential height perspective (panel
162 a) as well as in pressure (panel b) and potential temperature (panel c) space.

163 We use chemical observations obtained by several airborne instruments onboard
164 the M55 Geophysica for the diagnostic development herein. The measurements are sum-
165 marized in Table 1, and we direct the reader to the listed references for specifics about
166 the instruments. In the interest of being thorough, we include a few pertinent details be-
167 low.

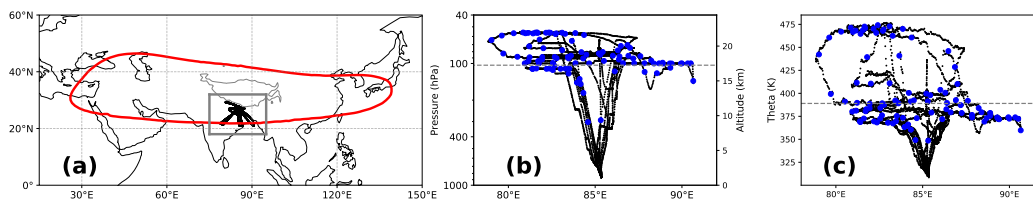


Figure 1. Setting of the StratoClim 2017 experiment with flight tracks shown in black. In panel a, the red contour shows the geopotential height contour of 16.77 km at 100 hPa (threshold taken from Bian et al., 2012) from Global Forecasting System (GFS) analysis averaged over the StratoClim measurement period, and the gray box shows the domain which the models are subset to throughout Section 3. Panels b and c show the flight tracks in vertical perspective using pressure, altitude and potential temperature vertical coordinates. Whole Air Sampler (WAS) observation points marked in blue, and dashed gray lines denote the mean tropopause during the StratoClim sampling period.

168 **2.1.1 AMICA Carbon Monoxide**

169 Observations of the tropospheric-sourced trace gas carbon monoxide (CO) are used
 170 to diagnose properties of convective transport. We use CO observations from the Air-
 171 borne Mid-Infrared Cavity enhanced Absorption spectrometer (AMICA, Kloss et al., 2021),
 172 which was deployed for the first time during the StratoClim campaign. These data are
 173 available on 10 second intervals, are estimated to have an overall accuracy of better than
 174 5% and a 1σ precision of ~ 20 ppb. These data have been previously analyzed toward
 175 understanding the dynamical and transport properties of the ASM by von Hobe et al.
 176 (2021).

177 **2.1.2 COLD2 Carbon Monoxide**

178 We also include CO observations from the Carbon Oxide Laser Detector 2 (COLD2,
 179 Viciani et al., 2018) instrument. COLD2 observations have a higher sampling frequency,
 180 with data available on a 1 second interval. The CO mixing ratio accuracy is estimated
 181 to be 3%. The COLD2 instrument has now been deployed for two ASM-centric campaigns:
 182 both StratoClim and the Asian summer monsoon Chemical and Climate Impact Project
 183 (ACCLIP 2022, Pan et al., 2022).

184 **2.1.3 FOZAN-II Ozone**

185 Ozone (O_3) is commonly used as a stratospheric tracer, making it an important
 186 component of the diagnostic development herein. We use observations of ozone taken
 187 from the Fast OZone ANalyzer (FOZAN-II, Yushkov et al., 1999; Ulanovsky et al., 2001)
 188 during six of the eight StratoClim flights in 2017. FOZAN-II sampling time is 1 second,
 189 the sensitivity is about 1 ppbv, and the average accuracy is 7%.

190 **2.1.4 HAGAR Nitrous Oxide**

191 We use observations of nitrous oxide (N_2O) due to its long tropospheric lifetime
 192 (15,600 years, SPARC Report No. 6), making it ideal to use as a chemical vertical co-
 193 ordinate in the stratosphere. This was measured during StratoClim by the High Alti-
 194 tude Gas AnalyzeR (HAGAR, Homan et al., 2010). The measurements have a 90 sec-
 195 ond sampling interval, an average precision of $\sim 0.5\%$ and an average accuracy of $\sim 0.6\%$.

196 **2.1.5 WAS Halogenated Species**

197 To assess the modeled chemical mechanisms, we make use of air samples collected
 198 by a Whole Air Sampler (WAS) during StratoClim, which were subsequently analyzed
 199 for a wide range of halogenated species (Adcock et al., 2021). Selected species for this
 200 study include methyl halides, (hydro)chlorofluorocarbons ((H)CFCs), with a focus on
 201 species emphasized in Adcock et al. (2021) due to their ready availability. These species
 202 are produced by both natural and anthropogenic activities, and if lofted to the strato-
 203 sphere can lead to the catalytic destruction of ozone. Each StratoClim flight included
 204 a maximum of 20 WAS samples, each with sampling duration of a few minutes. The sam-
 205 pling was performed on a non-uniform time grid, as depicted in Figure 1 (blue dots in
 206 panels b and c). Uncertainty information from each sample is provided via Adcock et
 207 al. (2021). “Merged” datasets onto the WAS measurement time interval are used in Sec-
 208 tion 3 to account for the irregular sampling intervals for this instrument. This is done
 209 by averaging all observations that fall between a given WAS canister’s open and close
 210 times.

211

2.2 Chemistry Transport Model Configurations

212

213

214

215

216

217

218

219

220

221

222

223

224

225

226

227

Use of the diagnostics developed herein is demonstrated using two atmosphere model components within the NCAR Community Earth System Model version 2 (CESM2, Danabasoglu et al., 2020). The first model is the Whole Atmosphere Community Climate Model version 6 (WACCM6, Gettelman et al., 2019) which uses a 0.95° latitude \times 1.25° longitude grid with 110 vertical levels spanning from the surface to ~ 140 km (Garcia and Richter, 2019). This vertical level configuration gives WACCM a vertical grid spacing of ~ 500 m in the UTLS. The second model is the recently-developed Multi-Scale Infrastructure for Chemistry and Aerosols version 0 (MUSICAv0, Schwantes et al., 2022), which has the capability for user-customized horizontal grid refinement to improve sampling over a region of interest. For the current work, a custom MUSICA grid is developed with refinement to ~ 30 km horizontal spacing over southeastern Asia and the western north Pacific (Figure S1a), while the remainder of the globe is covered by $\sim 1^\circ$ spacing (similar to WACCM). The MUSICA grid uses 32 vertical levels spanning from the surface to ~ 80 km (~ 3 hPa), resulting in a ~ 1 km vertical grid spacing in the UTLS. The vertical grid increments in WACCM and MUSICA are shown in Figure S1b. Output from the WACCM (MUSICA) simulation is available on 3- (6-) hour intervals.

228

229

230

231

232

233

234

235

236

Both WACCM and MUSICA utilize a specified dynamics option which nudges the temperature and zonal and meridional wind components to a chosen meteorological analysis. For this we use the Modern-Era Retrospective analysis for Research and Applications version 2 (MERRA-2, Gelaro et al., 2017). Global surface emissions are provided by the Copernicus Atmosphere Modeling System (CAM5, Granier et al., 2019). The chemistry mechanism in CESM2 includes a total of 231 species and 538 chemical reactions and is described by Emmons et al. (2020). The simulations parameterize deep convection using the Zhang-McFarlane scheme (Zhang & McFarlane, 1995). Other parameterizations are given by Gettelman et al. (2019) and are omitted here for brevity.

237

238

239

240

241

242

243

244

245

246

247

Advancements in computational processing and storage capabilities in recent years have enabled developments in finer grid spacing (i.e., higher resolution) and multi-scale grid capabilities in CTMs, such as MUSICA. In the present study, the MUSICA grid refinement is chosen to encompass the southern flank of the Tibetan Plateau (see Figure S1a), the primary “conduit” for ASM deep convective transport into the UTLS (e.g., Bergman et al., 2013; Honomichl & Pan, 2020; Clemens et al., 2023), with the intent to improve the representation of convective-scale processes responsible for lofting BL pollutants into the ASM UTLS. It remains unclear, however, whether improved grid point sampling necessarily improves a model’s performance compared to a coarser-grid counterpart. This supports the establishment of process-based model evaluation diagnostics as a timely research area.

248

249

250

251

252

253

254

255

256

257

258

259

260

261

262

To illustrate the important role of the ASM in modifying UTLS composition, Figure 2 shows global map sections of selected chemical species from WACCM valid 500 m above the local model tropopause. A pronounced chemical signature of trace gases associated with the ASM UTLS anticyclone can be seen, similar to that of past observational and modeling studies (e.g., Park et al., 2007; Randel et al., 2010; Munchak & Pan, 2014; Pan et al., 2022), but now with consideration for filtering for a “bulging” tropopause structure over the ASM (Pan et al., 2016). The result indicates that species with tropospheric lifetimes in months (top row) have mixing ratios in the lowermost stratosphere that are larger over the ASM than anywhere else on Earth, underscoring the potential for short-lived halogenated species emitted over Asia to impact the composition of the stratosphere via the ASM transport mechanism discussed in Section 1. In contrast, species with much longer tropospheric lifetimes (bottom row) show similar mixing ratio enhancements over south Asia as in the tropical tropopause layer (TTL, Fueglistaler et al., 2009). These species are well-mixed throughout the troposphere, but begin to decay in the lower stratosphere as transport times grow longer and their chemical sinks grow stronger. Their

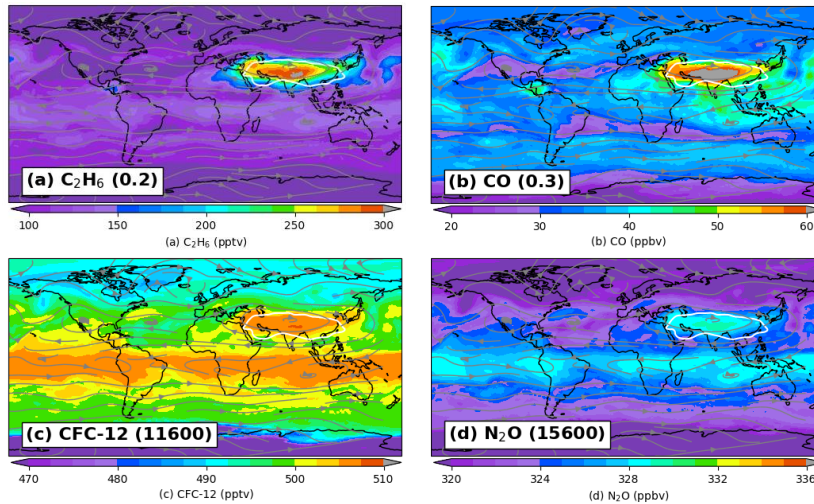
WACCM at 500m above the local tropopause

Figure 2. Plan views of WACCM model chemical species and dynamical variables in the lowermost stratosphere during the StratoClim observation period. Ethane (C_2H_6), carbon monoxide (CO), CFC-12 (CCl_2F_2) and nitrous oxide (N_2O) averaged from July 27 – August 10, 2017 and 500 m above the local WACCM tropopause are shown. White contours show WACCM tropopause altitudes greater than 16.77 km and gray lines show wind streamlines. Respective tropospheric lifetimes from SPARC Report No. 6 are given in parentheses.

263 highest mixing ratios in Figure 2 are simply regions where there is net upward transport
 264 across the tropopause: the TTL and the ASM.

265 **3 Process-based Diagnostic Development and Evaluation Demonstration**

267 **3.1 Transport by Monsoon Deep Convection**

268 Deep convection associated with the ASM is responsible for redistributing natu-
 269 ral and anthropogenic pollutants from the BL into the UTLS (e.g., Fu et al., 2006). In
 270 this section we use high-resolution airborne data to diagnose the convective param-
 271 eterization in WACCM and MUSICA (Zhang and McFarlane, 1995) by evaluating how well
 272 a tropospheric and stratospheric tracer (CO and ozone, respectively) are distributed through-
 273 out the free troposphere and UTLS compared to observations.

274 To examine vertical transport of CO and ozone, vertical distributions of the Stra-
 275 toClim observations and model results for South Asia are shown in Figure 3. Tracer mix-
 276 ing ratios are compared using two different vertical coordinates: adjusted tropopause-
 277 relative altitude, which expands the tropospheric layer and highlights the air mass tran-
 278 sition across the tropopause, and potential temperature, which collapses the tropospheric
 279 layer to highlight the transition between convective-dominated and radiative-dominated
 280 ascent processes. The lapse rate tropopause (LRT) altitude from ERA5 reanalysis (Hersbach
 281 et al., 2020; Hoffmann & Spang, 2022) is interpolated to the flight tracks for observa-
 282 tions, while the model-derived LRT is used for WACCM and MUSICA. The tropopause-
 283 relative altitude coordinate has utility for understanding the behavior of ASM convec-
 284 tive transport relative to the tropopause, and enables adjustment for subtle differences

285 between model dynamics and those in the real atmosphere. This analysis is complemen-
 286 tary to and extends that of von Hobe et al. (2021), by analyzing how models represent
 287 tracer behavior in the ASM region.

288 The result shows that MUSICA and WACCM have a generally good agreement with
 289 CO observations from AMICA and COLD2, mixing ratios ranging from ~ 70 -140 ppbv
 290 throughout the troposphere and gradually decreasing to ~ 15 -30 ppbv in the lower strato-
 291 sphere in both observations and models (Figure 3, left panels). CO observations have
 292 a similar distribution of CO throughout the majority of free tropospheric altitudes, sug-
 293 gesting that convection is the dominant transport process up to ~ 1 -2 km below the lo-
 294 cal tropopause (~ 15 km altitude on average). Separate maxima in modeled CO in the
 295 lower and upper troposphere show the influence of shallow and deep convective modes
 296 of transport, respectively. In potential temperature space, the noticeable discontinuity
 297 at ~ 360 K clearly reveals the transition from convective-dominated to radiative-dominated
 298 ascent.

299 On the other hand, MUSICA and WACCM struggle to represent the observed dis-
 300 tribution of ozone, with a high bias spanning between the free troposphere and lower strato-
 301 sphere (Figure 3, right panels). This is not particularly surprising, as WACCM and MU-
 302 SICA ozone has been noted to have a high bias in previous work when compared to ob-
 303 servations (Froidevaux et al., 2019; Dubé et al., 2022; Tang et al., 2023). Ozone mixing
 304 ratios observed by FOZAN-II are further supported by ozonesonde observations over Nepal
 305 during StratoClim, which show ~ 30 -50 ppbv ozone throughout the free troposphere (Brunamonti
 306 et al., 2018). We have performed several sensitivity experiments to elucidate the cause
 307 of the model high bias, including testing for sensitivity to chemistry of very short lived
 308 (VSL) species using the model configuration of Villamayor et al. (2023), and to adjust-
 309 ing the model’s lightning parameterization to generate less NO_x (an ozone precursor).
 310 The results of these sensitivity runs on model ozone mixing ratios shown in Figure S3.
 311 Although these experiments reduce the model’s ozone, they do not explain a sufficiently
 312 large bias to close the gap with the observations. More generally, these sensitivity ex-
 313 periments demonstrate another application of the dynamical coordinate diagnostic, high-
 314 lighting its utility in interrogating modeled representations of tracer mixing ratios.

315 A critical component to the analysis presented in Figure 3 is that model distribu-
 316 tions are computed from broader spatial and temporal boundaries compared to the Stra-
 317 toClim flight tracks. Specifically, the model distributions are an average of all grid points
 318 between 75-95°E longitude, 18-32°N latitude (the gray box printed on Figure 1a), and
 319 at every 3- or 6-hour interval between July 27 – August 10, 2017. Instead of comparing
 320 each observation to a much larger model grid cell through interpolation (we demonstrate
 321 this common technique in Figure S2 for context), our technique allows a comparison of
 322 the general behavior of ASM transport throughout the monsoon’s active phase. We ac-
 323 knowledge that flight campaigns often bias their sampling to specific phenomenon (e.g.,
 324 convective complexes, wildfire plumes, etc.) which could complicate the interpretation
 325 of this evaluation, however most StratoClim flights were designed to survey the large-
 326 scale characteristics of the ASM UTLS, which supports the compatibility of this eval-
 327 uation technique (Bucci et al., 2020).

328 To demonstrate an additional use of the dynamical vertical coordinates used in this
 329 analysis, we compare distributions of the tropospheric tracer CO in Figure 4 at key ver-
 330 tical layers identified from analyzing Figure 3. This allows for a more quantitative eval-
 331 uation of the models against the observations, as well as a quantitative comparison of
 332 the WACCM and MUSICA grid configurations following the discussion in Section 2.2.
 333 The general similarity between observations and models at each of the selected layers
 334 corroborates with the qualitative agreement noted in Figure 3. Mean values from the dis-
 335 tributions are collected in Table 2.

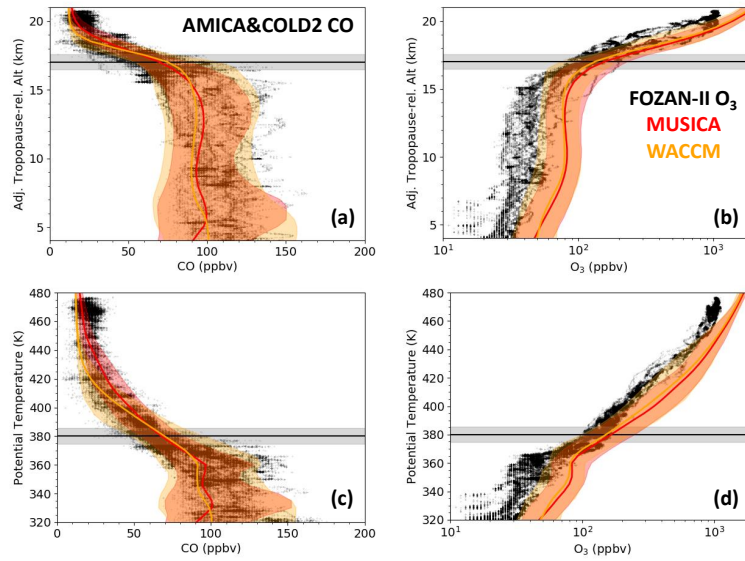


Figure 3. Vertical profile distributions of modeled and observed (left) CO and (right) ozone mixing ratio vertical profiles from models and StratoClim observations. The top panels are plotted in tropopause-relative altitude space while the bottom panels are plotted in potential temperature space. Black dots show StratoClim observations, and MUSICA (WACCM) results are plotted in red (orange), where solid lines show the mean and shaded regions show the 5th to 95th percentile range. The tropopause is denoted by the solid black line with its standard deviation marked by gray shading. Y-axes in the top panels are “adjusted” by the mean tropopause value for ease of comprehension. Model output is restricted to 75-95 E, 18-32 N (gray box in Figure 1a) from July 27 - August 10, 2017.

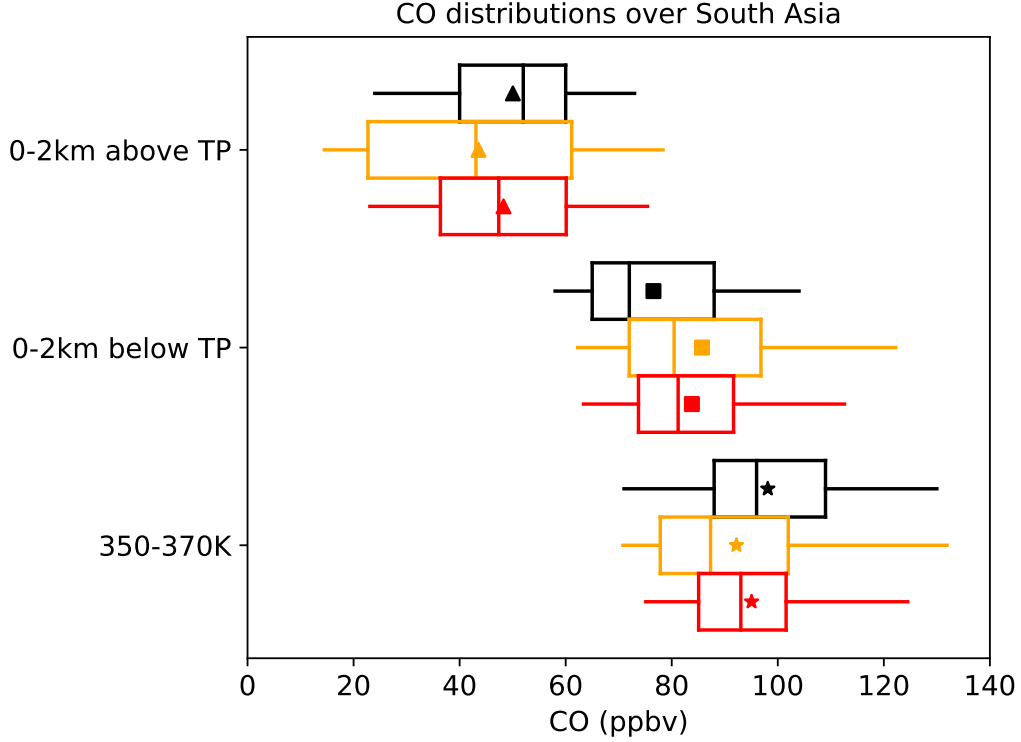


Figure 4. Box and whisker plots for CO mixing ratios within selected vertical ranges, with observations from AMICA and COLD2 in black, WACCM in orange, and MUSICA in red. “Boxes” span from the 25th to 75th percentiles, “whiskers” span from the 5th to 95th percentiles, and the vertical lines in the “boxes” represent the median. Mean mixing ratios are plotted as triangles (squares) for 0 to 2km above (below) the local tropopause (abbreviated as “TP” on the y axis), and as stars for 350 K to 370 K potential temperature.

336 There is no obvious advantage demonstrated by the MUSICA simulation with re-
 337 fined horizontal grid spacing at the level of primary convective outflow (stars in Figure
 338 4 and Table 2). This may be because convection must still be parameterized with the
 339 MUSICA grid configuration. Interestingly however, CO mixing ratios distributions in
 340 the lowermost stratosphere (triangles in Figure 4 and Table 2) suggest a low bias com-
 341 pared to observations. Although the present work does not pursue model improvements
 342 to address these discrepancies, the examples provided here are evidence for how the di-
 343 agnostics using these dynamical coordinates may identify specific areas for targeted model
 344 interrogation and development.

345 3.2 Transport Across the ASM Tropopause

346 Polluted air masses lofted by deep convection may be deposited higher than the
 347 level of zero radiative heating (LZRH, $\sim 360\text{K}$ in the tropics, Ploeger et al., 2010), above
 348 which air masses preferentially undergo comparatively slow ascent. Polluted air masses
 349 which cross the ASM tropopause, either vertically or through quasi-isentropic transport
 350 to the surrounding lower-tropopause regions (e.g., Pan et al., 2016; Vogel et al., 2019),
 351 may thus have the potential to impact global composition and climate. Modeling the ap-
 352 propriate mixing ratios of pollutants at the ASM tropopause is thus an important com-

Table 2. Mean CO mixing ratios (ppbv) in each selected vertical range shown in Figure 4.

Layer Symbol	0-2 km above LRT Triangle	0-2 km above LRT Square	350-370 K θ Star
AMICA/COLD2	43.2	69.4	98.1
WACCM	43.6	85.7	92.2
MUSICA	48.3	83.8	95.1

ponent of representing the ASM’s impacts. This section diagnoses the model representation of halogenated species and N₂O mixing ratios in the ASM tropopause layer.

Selected halogenated species and N₂O from WACCM, MUSICA, and StratoClim airborne observations from the WAS and HAGAR instruments (respectively) are shown in Figure 5. As in Section 3.1, we use an adjusted tropopause-relative coordinate to adjust for dynamical differences in models compared to that in the real atmosphere. The result shows that the models have qualitatively good representation of the four selected species at the ASM tropopause. For species with tropospheric lifetimes longer than one year, tropospheric mixing ratios are nearly constant with altitude given this is long compared to typical overturning of the troposphere (typically 2-3 weeks). Thus, their mixing ratio accuracy at the tropopause is mainly controlled by the model’s lower boundary condition used to prescribe surface mixing ratios. We note there is a slight high bias in modeled mixing ratios found ~2-3 km above the local tropopause in all panels of Figure 5. This suggests an error in the behavior of model dynamics in the lower stratosphere, either through vertical motion or mixing from the surrounding regions. The model representation of the lower stratosphere will be addressed in more detail in Section 3.3.

Although the modeled species tropopause mixing ratios depicted in Figure 5 are qualitatively encouraging, we wish to establish a quantitative diagnostic to characterize the error in modeled stratospheric entry mixing ratios, to easily identify species which are simulated (in)adequately. For this, we calculate the mean observed and modeled mixing ratios near the local tropopause (we choose within 1 km above and below; see the gray regions in Figure 5) and compare their difference against the “observational range of variability”, to characterize biases which are large compared to the mixing ratio range throughout the ASM UTLS. Put mathematically:

$$\text{Stratosphere Entry Error} = \frac{q_{t,m} - q_{t,o}}{\Delta q_o} * 100\% \quad (1)$$

where q is the mixing of a given specie, the subscript t indicates the mean mixing ratio within 1 km of the local tropopause (as shown in Figure 5) during the StratoClim period, and the subscript m (o) indicates modeled (observed). Δq_o is the difference between the maximum and minimum observed mixing ratio in the entire StratoClim dataset (i.e., the “observational range of variability”). The results are shown in Figure 6.

The calculation of error statistics, as done in Figure 6, provides a conceptual framework for identifying model skill in species representation, concisely highlighting areas where focused model development is needed. It also allows for different model configurations to be compared relative to one another. In the current approach, we see mostly superficial differences between WACCM and MUSICA in their stratospheric entry mixing ratio performance, likely a consequence of the same emissions database used in the simulations. Most species have stratospheric entry mixing ratio errors which are less than 10%, which we consider to be small given they could be easily explained by a combination of measurement and model uncertainties as well as the intentional sampling differ-

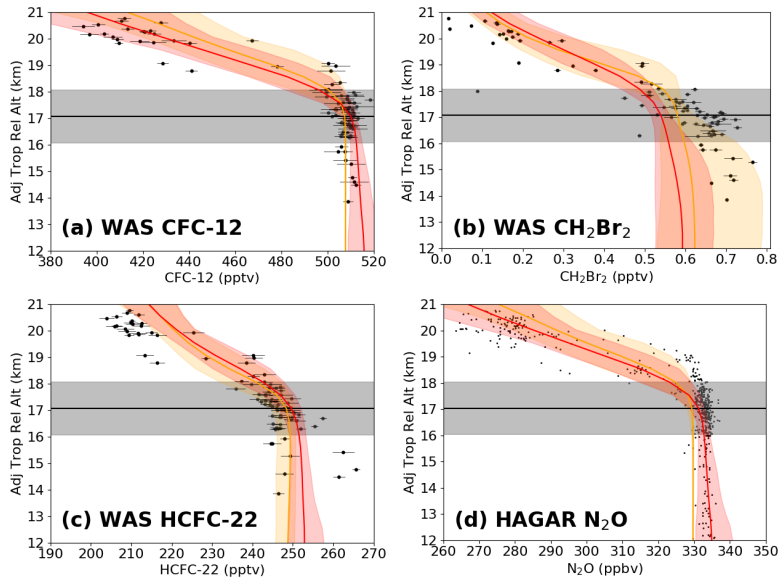


Figure 5. Modeled and observed vertical profiles of selected chemical species plotted in adjusted tropopause-relative altitude space. Black dots show observations with uncertainty plotted in thin horizontal lines. The red (orange) line shows the mean profile from the MUSICA (WACCM) simulation between 75-95E and 18-32N (the small gray box in Figure 1) from July 27 - August 10, 2017, with the corresponding shading spanning the 5th to 95th percentiles. The mean tropopause is shown as a black line, with the range of 1 km below and above it (used for calculation of the “stratospheric entry value”) shaded in gray. As in Figure 3, y-axes are “adjusted” to the mean tropopause altitude for ease of comprehension.

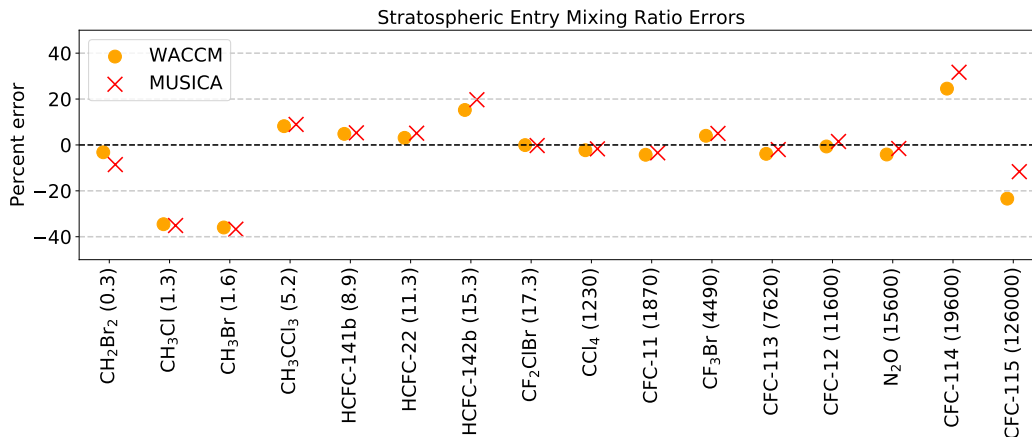


Figure 6. A scatterplot of model stratospheric entry errors for selected species. Species are sorted by their tropospheric lifetimes (SPARC Report No. 6) which are printed in parentheses in units of years.

ences we use to avoid space-time interpolation. However, this diagnostic identifies methyl chloride (CH₃Cl), methyl bromide (CH₃Br), CFC-114, and CFC-115 as species with larger errors which may have other contributing factors. Methyl chloride and bromide are of particular interest because although their tropospheric lifetimes are on the order of one year, their stratospheric lifetimes are on the order of decades (SPARC Report No. 6, Ko et al., 2013). Since these species will persist in the stratosphere for decades if they can penetrate the tropopause, and because of their impacts on stratospheric ozone chemistry (e.g., Bednarz et al., 2022), their mixing ratios in the ASM UTLS are especially important to properly represent.

To demonstrate the use of the stratospheric entry mixing ratio error calculation (Equation 1; Figure 6) in diagnosing model shortcomings, Figure 7 shows the methyl halides plotted in chemical vertical coordinate space. Both CO and CFC-12 are used as chemical coordinates to expand the tropospheric and stratospheric layers, respectively. The noticeable offsets between observed mixing ratios (black) and those from the models (red and orange) corroborate with their large errors (Figure 6). With the exception of dibromomethane (CH₂Br₂) which has the shortest tropospheric lifetime in this study, all the species analyzed in Figure 6 have mixing ratios prescribed at the model surface by using zonally-averaged mole fraction boundary conditions. Species with sufficiently long lifetimes relative to tropospheric overturning are expected to have nearly-uniform mixing ratios throughout the troposphere, as demonstrated by WACCM in Figure 2. However, for species with shorter tropospheric lifetimes such as methyl chloride and methyl bromide, this lower boundary condition may obscure important regional emissions sources, such as those from Asia, and lead to an underestimation of their composition and climate impact potentials.

The hypothesis that zonally-averaged mole fraction surface boundary conditions causes errors for methyl chloride and bromide at the stratospheric entry point can be further investigated by comparing WACCM and MUSICA results with observations outside the ASM region. For this we include in Figure 7 observations from the Studies of Emissions and Atmospheric Composition, Clouds and Climate Coupling by Regional Surveys (SEAC⁴RS) campaign, which took place over North America during boreal summer 2013 (Toon et al., 2016), as gray dots. SEAC⁴RS observations align nicely with the 2017 WACCM and MUSICA simulations subset to the ASM region (gray box in Figure

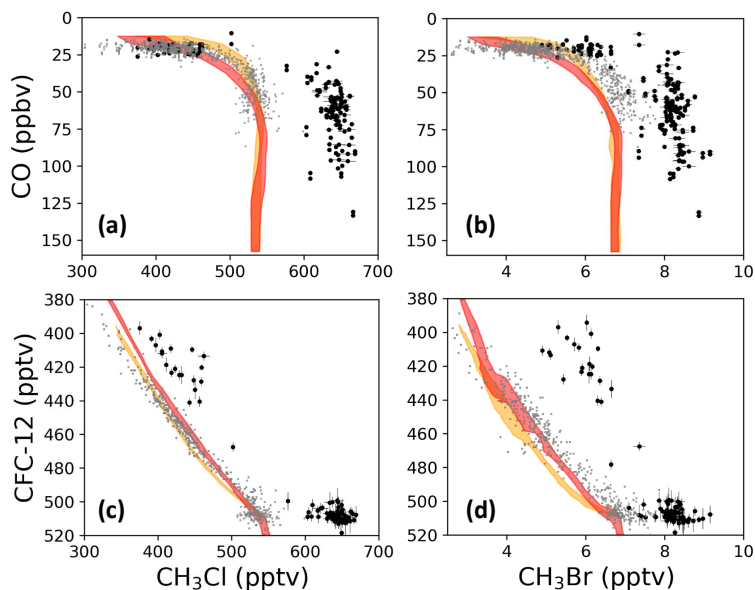


Figure 7. Vertical profiles of (left) methyl chloride and (right) methyl bromide in chemical coordinate space using (top) CO and (bottom) CFC-12 as the vertical coordinates. WACCM (MUSICA) mixing ratios from the 5th to 95th percentiles are shown in orange (red). Black dots show airborne observations from StratoClim (2017) with uncertainty bars, and gray dots show airborne observations from SEAC⁴RS 2013 (Toon et al., 2016) taken over North America. To ensure compatibility between the campaigns, we adjust the CFC-12 mixing ratios from SEAC⁴RS according to the long-term trend between 2013 and 2017, using observations from the NOAA/GML halocarbons program (Dutton et al., 2023).

423 1), indicating that model mixing ratios reflect the ASM’s surroundings rather than the
 424 ASM environment itself. This supports our assertion that the prescribed zonally-averaged
 425 boundary condition assumption breaks down for species with tropospheric lifetimes less
 426 than a few years. More broadly, this analysis highlights the value of the stratospheric
 427 entry diagnostic at identifying model shortcomings and providing a pathway for focused
 428 improvements.

429 3.3 Chemical Loss in the Lower Stratosphere

430 The two previous sub-sections focus on transport of Asian pollution into the UT
 431 via convective transport (Section 3.1), and subsequent entry to the stratosphere (Sec-
 432 tion 3.2). In this sub-section we diagnose the model representation of chemical loss pro-
 433 cesses in the lower stratosphere, using a “chemical vertical coordinate.” The relatively
 434 coarse vertical grid spacing in MUSICA which degrades further in the lower stratosphere
 435 (Figure S1b) leads us to focus this evaluation on the WACCM simulation only. Further-
 436 more, due to the aforementioned issues with methyl halide species (Figures 6 and 7) and
 437 the inappropriateness of a linear fit for dibromomethane (CH_2Br_2 ; not shown), these species
 438 are excluded from this chemical loss analysis.

439 Following the approach of Avallone and Prather (1997), a collection of tracer rela-
 440 tionships for halogenated species and N_2O are plotted in Figure 8 with CFC-12 mix-
 441 ing ratio used as the vertical coordinate for both WACCM and StratoClim observations.
 442 Although the full range of variability is plotted, we focus on the cluster of stratospheric
 443 observations between 394-442 pptv of CFC-12, to ensure the tracer relationships are con-

444 sistent with the observations. For this range of mixing ratios, linear “best fit” lines are
 445 calculated for both observations (black lines) and WACCM (brown lines). Measurement
 446 uncertainty (from Adcock et al., 2021) is accounted for by assigning weights to each point
 447 for the linear fitting, equal to the inverse of the sum of both the squared mixing ratio
 448 uncertainties. Furthermore, we discard two WAS data points (one for CCl₄ and another
 449 for CFC-114) which are clear outliers, and by inspection disrupt the appropriateness of
 450 the linear fit (not shown).

451 From the foundational arguments of Plumb and Ko (1992) on tracer relationships:
 452 “the curve becomes linear in any region if the net upward fluxes of two species through
 453 the rapid exchange surfaces in that region are in constant ratio.” Indeed, the modeled
 454 and observed relationships exhibit linear behavior in the lower stratosphere (Figure 8),
 455 suggesting the species lifetimes are long in this layer compared to the timescales of net
 456 upward flux. From a conceptual standpoint, the chemical mechanism in WACCM has
 457 excellent representation of this behavior. In contrast, many relationships in Figure 8 ex-
 458 hibit non-linear behavior closer to the tropopause (~ 500 pptv of CFC-12; see Figure 5),
 459 a consequence of the large lifetime disparity between the species on each axis. Often in
 460 these cases, the observations (gray dots) are considerably less compact than both WACCM
 461 (light orange dots) and their deeper stratospheric counterparts (black dots).

462 To quantify the ability of WACCM to represent the observed tracer relationships,
 463 a diagnostic is developed that is based on the modeled and observed chemical loss rate
 464 (i.e. slopes of the linear fitting). Often the WACCM loss rates are similar to those ob-
 465 served, but are “offset” in absolute mixing ratio (Figure 8). To calculate the loss rate
 466 and mixing ratio offset errors, we employ similar formulas as Equation 1 for the strato-
 467 spheric entry mixing ratio errors:

$$Loss\ Rate\ Error = \frac{m_{ls,W} - q_{ls,o}}{\Delta m_{ls,0}} * 100\% \quad (2)$$

$$Mixing\ Ratio\ Offset\ Error = \frac{q_{ls,W} - q_{ls,o}}{\Delta q_{ls,o}} * 100\% \quad (3)$$

468 In Equations 2 and 3, the subscript *ls* denotes the selected lower stratospheric range,
 469 *m* indicates the slope of the linear relationships, *q* indicates the x-axis tracer mixing ra-
 470 tio at the midpoint of the lower stratospheric range considered (i.e., 418 pptv of CFC-
 471 12), and subscripts *W* and *o* indicate modeled by WACCM and observed, respectively.
 472 The diagnostics in Equations 2 and 3 enable a quantitative evaluation of WACCM’s per-
 473 formance at representing the observed tracer relationships, separating the model repre-
 474 sentation of lower stratospheric dynamics and chemistry from offsets in the absolute mix-
 475 ing ratios found there.

476 To demonstrate the application of the loss rate and mixing ratio error diagnostics
 477 defined here, Figure 9 shows calculated results for the choice of two chemical vertical co-
 478 ordinates and two model domain selections. The selected vertical coordinates are CFC-
 479 12 (Figure 8) and N₂O (Figure S4, for which a range of 265-292 ppbv is chosen for the
 480 lower stratosphere). The two domain selections are that shown in the gray box in Fig-
 481 ure 1 (75-95E, 18-32N; denoted “small”), which is used throughout Sections 3.1 and 3.2,
 482 and a larger domain which approximately represents the ASM UTLS anticyclone (30-
 483 130E, 18-40N; denoted “large”).

484 The mixing ratio offset diagnostic (Equation 3) shows errors for all species which
 485 are less than 20% (Figure 9a), which is conceptually consistent with the stratospheric
 486 entry diagnostic presented in Section 3.2 (Figure 6). Indeed, a species with an accurate
 487 mixing ratio at the tropopause is predisposed to an accurate mixing ratio in the lower
 488 stratosphere. While the loss rate diagnostic (Equation 2; Figure 9b) also shows errors
 489 of less than 20% for most relationships, it identifies CFC-114 and CFC-115 as species

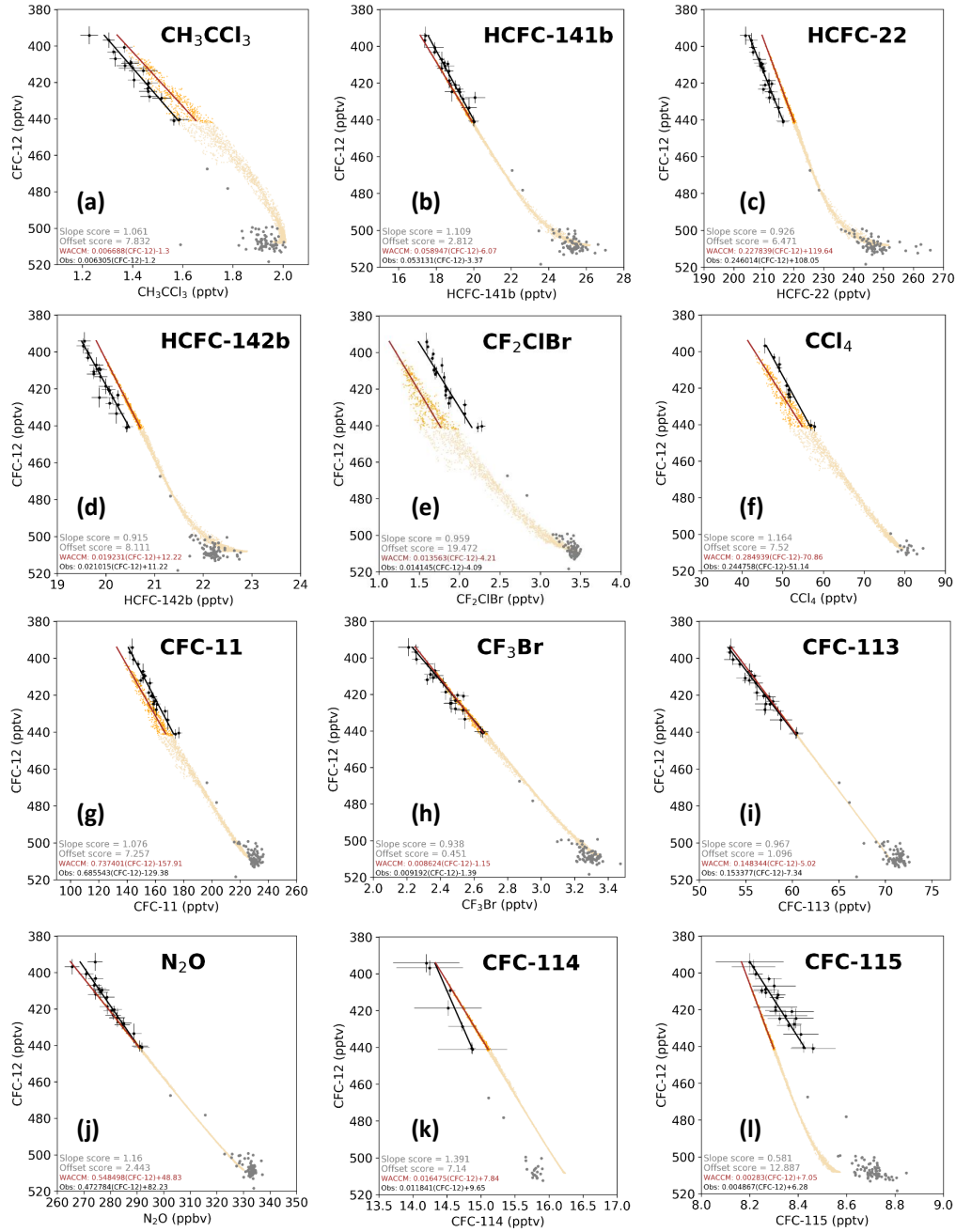


Figure 8. Various halocarbon and N_2O profiles in CFC-12 chemical vertical coordinate space. Black dots show StratoClim observations in the lower stratosphere ($394 \text{ pptv} < \text{CFC-12} < 442 \text{ pptv}$), with thin lines marking observational uncertainty. Thick black lines mark observational best-fits using a weighted linear regression. WACCM is shown in orange, with brown lines marking the linear model best-fit in the lower stratosphere. WACCM is subset between 78-92E, 18-32N (the small gray box in Figure 1), from July 27 - August 10, 2017, to 50-200 hPa to focus on the UTLS, and to every 50th point for visual clarity. Light orange and gray dots show model and observation points (respectively) near and below the tropopause, which are not used for the linear fitting.

490 with considerable deviations from the observed loss rates in chemical coordinate space.
 491 These deviations in loss rate, coupled with their poor stratospheric entry mixing ratio
 492 representation (Figure 6), are evidence that WACCM does not properly represent them.
 493 For both CFC-114 and CFC-115, loss by O^1D is an important process in comparison to
 494 loss by photolysis (from SPARC Report No. 6, 2013), which we highlight using aster-
 495 isks in the Figure 9 labeling. With this in mind, we find it reasonable to hypothesize that
 496 the model ozone high bias noted in Section 3.1 (Figure 3) contributes to the errors in
 497 these relationships, as ozone is the main source of O^1D in the lower stratosphere. A sub-
 498 sequent model experiment was performed with a longer spin-up to test for sensitivity in
 499 CFC-114 and CFC-115 given their relatively long stratospheric lifetimes, which did not
 500 yield improvements to this relationship (not shown).

501 We clarify again that it is not our objective to make corrections to the chemical
 502 mechanisms in the present work, only to show the utility of this diagnostic framework
 503 for identifying areas for focused model improvement. Investigating the shortcomings of
 504 these relationships are the subject of ongoing work, and may require the use of idealized
 505 chemical modeling to understand the complex mechanisms contributing to these rela-
 506 tionships.

507 With the use of the stratospheric mixing ratio offset and chemical loss rate diag-
 508 nostics in this subsection, we demonstrate that WACCM chemistry overall performs well
 509 at representing the chemical relationships observed during StratoClim. As with prior anal-
 510 yses, this diagnostic minimizes the impact of fundamental air mass size disparities be-
 511 tween observed and modeled air masses. Both diagnostics show a general consistency
 512 between the two choices of chemical vertical coordinate as well as the two choices of do-
 513 main. The consistency between the two domain choices suggests that the ASM anticy-
 514 clone has a composition signature in the lower stratosphere that is fairly consistent through-
 515 out; despite the StratoClim campaign spanning only a modest portion of the ASM UTLS
 516 anticyclone.

517 4 Conclusions and Outlook

518 In this study we design a set of process-based diagnostics using airborne in situ chem-
 519 ical tracer measurements to evaluate the representation of UTLS composition under the
 520 influence of ASM dynamics and transport. The diagnostics are:

- 521 1. The use of tropopause-relative altitude and potential temperature vertical coord-
 522 inates to evaluate distributions of tropospheric and stratospheric tracers (Sec-
 523 tion 3.1). These coordinates adjust for dynamical differences between models and
 524 the real atmosphere, and allow for the properties of modeled and observed con-
 525 vection to be diagnosed.
- 526 2. The use of a tropopause-relative altitude vertical coordinate to evaluate strato-
 527 spheric entry mixing ratios of chemical species (Section 3.2). For species with tro-
 528 pospheric lifetimes which are long compared to typical tropospheric overturning
 529 time scales, this diagnoses the representation of the mixing ratio boundary con-
 530 dition used at the model surface.
- 531 3. The use of long-lived tracers as a vertical coordinate to diagnose chemical loss pro-
 532 cesses in the lower stratosphere (Section 3.3). The application of this to a wide
 533 range of species identifies those which may have issues in their chemical treatment
 534 by the model.

535 We demonstrate the application of the above diagnostics in two global climate mod-
 536 els run in CTM configuration (WACCM and MUSICA) using airborne in situ observa-
 537 tions from the ASM region (StratoClim 2017). The exercise leads to the following con-
 538 clusions about the representation of ASM composition by WACCM and MUSICA:

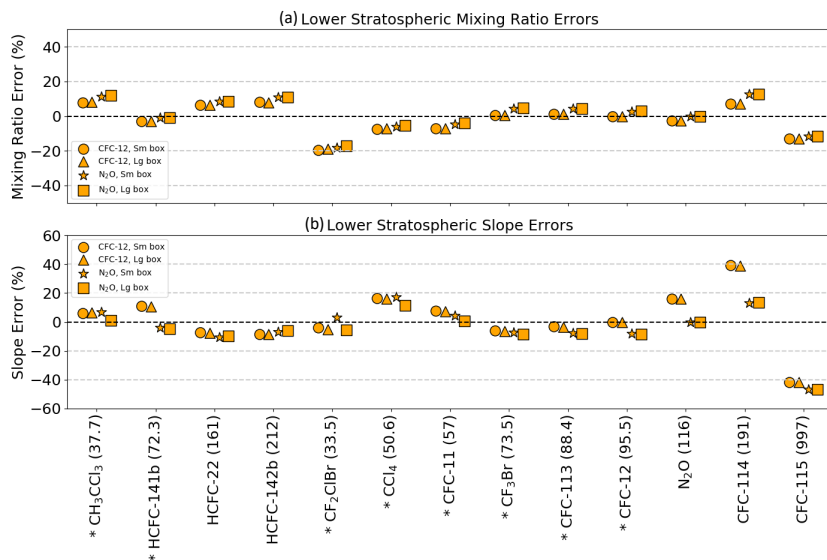


Figure 9. Scatterplots showing (a) mixing ratio errors and (b) loss rate errors between observations and models in the lower stratosphere. Symbols show calculations using CFC-12 and N_2O as the choice of chemical vertical coordinate, as well as two model domain choices (see text for details). Species are organized in the same order as Figure 6, but with their stratospheric lifetimes in years (SPARC Report No. 6) now printed in parentheses instead. Asterisks mark species whose loss is primarily controlled by photolysis.

- 539
- 540
- 541
- 542
- 543
- 544
- 545
- 546
- 547
- 548
- 549
- 550
- 551
- 552
- 553
- 554
- 555
- The level of ASM deep convective outflow ($\sim 15\text{km}$; $\sim 360\text{K}$) and distribution of CO observed during StratoClim are generally well-represented by WACCM and MUSICA. Both models show similar CO mixing ratios in key altitude ranges, despite differences in their horizontal and vertical grid increments. However, there is a high model bias in ozone throughout the free troposphere.
 - Observed tracer mixing ratios at the ASM tropopause are generally consistent with those in WACCM and MUSICA. For species with relatively short tropospheric lifetimes (less than a couple of years), representing mole fraction boundary conditions with a zonal average obscures important regional emissions sources which may lead to large model biases, as shown to be the case for methyl chloride and methyl bromide.
 - The use of long-lived chemical vertical coordinates reveals that WACCM represents the compact nature of chemical relationships observed in the lower stratosphere. Species whose stratospheric loss rates are dominated by photolysis have particularly good agreement in their chemical loss rates compared to observations, while the high model ozone bias may negatively impact the representation of loss for other species.

556

557

558

559

560

561

562

Climate prediction is often conducted on spatial scales of hundreds of kilometers and temporal scales of decades, but accurate prediction at these scales requires accurate representation of embedded smaller-scale processes which are captured by the high spatial and temporal sampling of airborne observations. The diagnostic development and the resulting evaluation of NCAR CESM configurations herein thus highlights the irreplaceable value of airborne observations toward improving Earth system modeling capabilities. Moreover, the diagnostics are designed to minimize the fundamental differ-

563 ences in air mass sizes represented by models and observations, as compared to a typ-
564 ical method of space-time interpolation.

565 The establishment of this diagnostic framework may help realize the benefits, and
566 even shortcomings, of ongoing CTM developments. Future work will examine the per-
567 formance of modeling capabilities at representing a recent set of ASM airborne obser-
568 vations taken during the ACCLIP 2022 campaign (Pan et al., 2022). We note that al-
569 though these diagnostics are designed specifically with an ASM UTLS focus, we expect
570 them to be appropriate for other regions of the globe to evaluate their respective trans-
571 port regimes.

572 5 Open Research

573 The Community Earth System Model (CESM) is an open-source community model
574 available from <http://www.cesm.ucar.edu/>. The Whole Atmosphere Community Climate
575 Model (WACCM) is described by <https://www2.acom.ucar.edu/gcm/waccm>, and the
576 Multi-scale Infrastructure for Chemistry and Aerosols (MUSICA) is described by

577 <https://wiki.ucar.edu/display/MUSICA/MUSICA+Home>. StratoClim data will
578 be accessible via the HALO database at <https://halo-db.pa.op.dlr.de/mission/101>. Un-
579 til this time, it can be provided by request from the respective instrument PIs (see Ta-
580 ble 1). SEAC⁴RS observations are available from

581 <https://www-air.larc.nasa.gov/cgi-bin/ArcView/seac4rs>. ERA5 reanalysis (doi: 10.5065/P8GT-
582 0R61) is available from the NCAR CISL Research Data Archive.

583 Acknowledgments

584 The National Center for Atmospheric Research (NCAR) is supported by the National
585 Science Foundation (NSF). W.P.S. was supported under grant NSF AGS-1853929. K.E.A.
586 was funded by the UK Natural Environment Research Council through the EnvEast Doc-
587 toral Training Partnership (grant number NE/L002582/1). We acknowledge high-performance
588 computing support from Cheyenne (<https://doi.org/10.5065/D6RX99HX>) provided by
589 NCAR’s Computational and Information Systems Laboratory (CISL), sponsored by the
590 NSF. Airborne measurements were made possible by European Community’s Seventh
591 Framework Programme (FP7/2007–2013), grant agreement 603557—Project STRATO-
592 CLIM. We acknowledge support from the Geophysica aircraft team, the StratoClim sci-
593 ence team and the NCAR multi-scale modeling community, as well as helpful comments
594 from M. Barth, W. Randel and E. Weatherhead.

595 References

- 596 Adcock, K. E., Fraser, P. J., Hall, B. D., Langenfelds, R. L., Lee, G., Montzka,
597 S. A., . . . others (2021). Aircraft-based observations of ozone-depleting sub-
598 stances in the upper troposphere and lower stratosphere in and above the asian
599 summer monsoon. *Journal of Geophysical Research: Atmospheres*, 126(1),
600 e2020JD033137.
- 601 Avallone, L. M., & Prather, M. J. (1997). Tracer-tracer correlations: Three-
602 dimensional model simulations and comparisons to observations. *Journal*
603 *of Geophysical Research: Atmospheres*, 102(D15), 19233–19246.
- 604 Bednarz, E. M., Hossaini, R., Chipperfield, M. P., Abraham, N. L., & Braesicke, P.
605 (2022). Atmospheric impacts of chlorinated very short-lived substances over
606 the recent past—part 1: Stratospheric chlorine budget and the role of transport.
607 *Atmospheric Chemistry and Physics*, 22(16), 10657–10676.
- 608 Bergman, J. W., Fierli, F., Jensen, E. J., Honomichl, S., & Pan, L. L. (2013).
609 Boundary layer sources for the asian anticyclone: Regional contributions to
610 a vertical conduit. *Journal of Geophysical Research: Atmospheres*, 118(6),

- 611 2560–2575.
- 612 Bian, J., Pan, L. L., Paulik, L., Vömel, H., Chen, H., & Lu, D. (2012). In situ water
613 vapor and ozone measurements in lhasa and kunming during the asian summer
614 monsoon. *Geophysical Research Letters*, *39*(19).
- 615 Bossolasco, A., Jegou, F., Sellitto, P., Berthet, G., Kloss, C., & Legras, B. (2021).
616 Global modeling studies of composition and decadal trends of the asian
617 tropopause aerosol layer. *Atmospheric Chemistry and Physics*, *21*(4), 2745–
618 2764.
- 619 Brunamonti, S., Jorge, T., Oelsner, P., Hanumanthu, S., Singh, B. B., Kumar, K. R.,
620 ... others (2018). Balloon-borne measurements of temperature, water vapor,
621 ozone and aerosol backscatter on the southern slopes of the himalayas
622 during stratoclim 2016–2017. *Atmospheric Chemistry and Physics*, *18*(21),
623 15937–15957.
- 624 Bucci, S., Legras, B., Sellitto, P., d’Amato, F., Viciani, S., Montori, A., ... others
625 (2020). Deep-convective influence on the upper troposphere–lower strato-
626 sphere composition in the asian monsoon anticyclone region: 2017 stratoclim
627 campaign results. *Atmospheric Chemistry and Physics*, *20*(20), 12193–12210.
- 628 Chen, B., Xu, X., Yang, S., & Zhao, T. (2012). Climatological perspectives of air
629 transport from atmospheric boundary layer to tropopause layer over asian
630 monsoon regions during boreal summer inferred from lagrangian approach.
631 *Atmospheric Chemistry and Physics*, *12*(13), 5827–5839.
- 632 Clemens, J., Vogel, B., Hoffmann, L., Griessbach, S., Thomas, N., Fadnavis, S., ...
633 Ploeger, F. (2023). Identification of source regions of the asian tropopause
634 aerosol layer on the indian subcontinent in august 2016. *EGUsphere*, *2023*,
635 1–39.
- 636 Danabasoglu, G., Lamarque, J.-F., Bacmeister, J., Bailey, D., DuVivier, A., Ed-
637 wards, J., ... others (2020). The community earth system model ver-
638 sion 2 (cesm2). *Journal of Advances in Modeling Earth Systems*, *12*(2),
639 e2019MS001916.
- 640 Dethof, A., O’neill, A., Slingo, J., & Smit, H. (1999). A mechanism for moistening
641 the lower stratosphere involving the asian summer monsoon. *Quarterly Journal*
642 *of the Royal Meteorological Society*, *125*(556), 1079–1106.
- 643 Dubé, K., Randel, W., Bourassa, A., & Degenstein, D. (2022). Tropopause-level
644 nox in the asian summer monsoon. *Geophysical Research Letters*, *49*(18),
645 e2022GL099848.
- 646 Dutton, G. S., Hall, B. D., Montzka, S. A., & Nance, J. D. (2023). Combined
647 atmospheric chlorofluorocarbon-12 dry air mole fractions from the noaa gml
648 halocarbons sampling network, 1977-2023. [https://doi.org/10.15138/PJ63-
649 H440](https://doi.org/10.15138/PJ63-H440).
- 650 Emmons, L., Schwantes, R. H., Orlando, J. J., Tyndall, G., Kinnison, D., & Lamar-
651 que, J.-F. e. a. (2020). The chemistry mechanism in the community earth
652 system model version 2 (cesm2). *Journal of Advances in Modeling Earth*
653 *Systems*.
- 654 Fan, Q., Bian, J., & Pan, L. L. (2017). Stratospheric entry point for upper-
655 tropospheric air within the asian summer monsoon anticyclone. *Science China*
656 *Earth Sciences*, *60*, 1685–1693.
- 657 Fernandez, R. P., Barrera, J. A., López-Noreña, A. I., Kinnison, D. E., Nicely,
658 J., Salawitch, R. J., ... others (2021). Intercomparison between sur-
659rogate, explicit, and full treatments of vsl bromine chemistry within the
660 cam-chem chemistry-climate model. *Geophysical Research Letters*, *48*(4),
661 e2020GL091125.
- 662 Froidevaux, L., Kinnison, D. E., Wang, R., Anderson, J., & Fuller, R. A. (2019).
663 Evaluation of cesm1 (waccm) free-running and specified dynamics atmospheric
664 composition simulations using global multispecies satellite data records. *Atmo-
665 spheric Chemistry and Physics*, *19*(7), 4783–4821.

- 666 Fu, R., Hu, Y., Wright, J. S., Jiang, J. H., Dickinson, R. E., Chen, M., . . . Wu,
667 D. L. (2006). Short circuit of water vapor and polluted air to the global strato-
668 sphere by convective transport over the tibetan plateau. *Proceedings of the*
669 *National Academy of Sciences*, *103*(15), 5664–5669.
- 670 Fueglistaler, S., Dessler, A., Dunkerton, T., Folkins, I., Fu, Q., & Mote, P. W.
671 (2009). Tropical tropopause layer. *Reviews of Geophysics*, *47*(1).
- 672 Gelaro, R., McCarty, W., Suárez, M. J., Todling, R., Molod, A., Takacs, L., . . .
673 others (2017). The modern-era retrospective analysis for research and applica-
674 tions, version 2 (merra-2). *Journal of climate*, *30*(14), 5419–5454.
- 675 Gettelman, A., Mills, M., Kinnison, D., Garcia, R., Smith, A., Marsh, D., . . . others
676 (2019). The whole atmosphere community climate model version 6 (waccm6).
677 *Journal of Geophysical Research: Atmospheres*, *124*(23), 12380–12403.
- 678 Granier, C., Darras, S., Denier van Der Gon, H., Doubalova, J., Elguindi, N., Galle,
679 B., . . . others (2019). The copernicus atmosphere monitoring service global
680 and regional emissions. *Reading, United Kingdom: Copernicus Atmosphere*
681 *Monitoring Service*. <https://doi.org/10.24380/d0bn-kx16>.
- 682 Hersbach, H., Bell, B., Berrisford, P., Hirahara, S., Horányi, A., Muñoz-Sabater, J.,
683 . . . others (2020). The era5 global reanalysis. *Quarterly Journal of the Royal*
684 *Meteorological Society*, *146*(730), 1999–2049.
- 685 Hoffmann, L., & Spang, R. (2022). An assessment of tropopause characteristics
686 of the era5 and era-interim meteorological reanalyses. *Atmospheric Chemistry*
687 *and Physics*, *22*(6), 4019–4046.
- 688 Homan, C., Volk, C., Kuhn, A., Werner, A., Baehr, J., Viciani, S., . . . Ravegnani,
689 F. (2010). Tracer measurements in the tropical tropopause layer during the
690 amma/scout-o3 aircraft campaign. *Atmospheric Chemistry and Physics*, *10*(8),
691 3615–3627.
- 692 Honomichl, S. B., & Pan, L. L. (2020). Transport from the asian summer monsoon
693 anticyclone over the western pacific. *Journal of Geophysical Research: Atmo-*
694 *spheres*, *125*(13), e2019JD032094.
- 695 Kloss, C., Tan, V., Leen, J. B., Madsen, G. L., Gardner, A., Du, X., . . . others
696 (2021). Airborne mid-infrared cavity enhanced absorption spectrometer (am-
697 ica). *Atmospheric Measurement Techniques*, *14*(8), 5271–5297.
- 698 Ko, M. K., Newman, P. A., Reimann, S., Strahan, S. E., Atlas, E. L., Burkholder,
699 J. B., . . . others (2013). Recommended values for steady-state atmospheric
700 lifetimes and their uncertainties. *SPARC Report on the Lifetimes of Strato-*
701 *spheric Ozone-Depleting Substances, Their Replacements, and Related Species*.
- 702 Krishnamurti, T. N., & Bhalme, H. (1976). Oscillations of a monsoon system. part i.
703 observational aspects. *Journal of Atmospheric Sciences*, *33*(10), 1937–1954.
- 704 Legras, B., & Bucci, S. (2020). Confinement of air in the asian monsoon anticyclone
705 and pathways of convective air to the stratosphere during the summer season.
706 *Atmospheric Chemistry and Physics*, *20*(18), 11045–11064.
- 707 Munchak, L. A., & Pan, L. L. (2014). Separation of the lapse rate and the cold
708 point tropopauses in the tropics and the resulting impact on cloud top-
709 tropopause relationships. *Journal of Geophysical Research: Atmospheres*,
710 *119*(13), 7963–7978.
- 711 Pan, L. L., Atlas, E. L., Salawitch, R., Honomichl, S., Bresch, J., Randel, W., . . .
712 others (2017). The convective transport of active species in the tropics (con-
713 trast) experiment. *Bulletin of the American Meteorological Society*, *98*(1),
714 106–128.
- 715 Pan, L. L., Bowman, K. P., Atlas, E. L., Wofsy, S. C., Zhang, F., Bresch, J. F., . . .
716 others (2010). The stratosphere–troposphere analyses of regional transport
717 2008 experiment. *Bulletin of the American Meteorological Society*, *91*(3),
718 327–342.
- 719 Pan, L. L., Honomichl, S. B., Kinnison, D. E., Abalos, M., Randel, W. J., Bergman,
720 J. W., & Bian, J. (2016). Transport of chemical tracers from the bound-

- ary layer to stratosphere associated with the dynamics of the asian summer monsoon. *Journal of Geophysical Research: Atmospheres*, 121(23), 14–159.
- Pan, L. L., Kinnison, D., Liang, Q., Chin, M., Santee, M. L., Flemming, J., . . . others (2022). A multimodel investigation of asian summer monsoon utls transport over the western pacific. *Journal of Geophysical Research: Atmospheres*, 127(24), e2022JD037511.
- Park, M., Randel, W. J., Gettelman, A., Massie, S. T., & Jiang, J. H. (2007). Transport above the asian summer monsoon anticyclone inferred from aura microwave limb sounder tracers. *Journal of Geophysical Research: Atmospheres*, 112(D16).
- Park, M., Randel, W. J., Kinnison, D. E., Garcia, R. R., & Choi, W. (2004). Seasonal variation of methane, water vapor, and nitrogen oxides near the tropopause: Satellite observations and model simulations. *Journal of Geophysical Research: Atmospheres*, 109(D3).
- Ploeger, F., Konopka, P., Günther, G., Groöß, J.-U., & Müller, R. (2010). Impact of the vertical velocity scheme on modeling transport in the tropical tropopause layer. *Journal of Geophysical Research: Atmospheres*, 115(D3).
- Ploeger, F., Konopka, P., Walker, K., & Riese, M. (2017). Quantifying pollution transport from the asian monsoon anticyclone into the lower stratosphere. *Atmospheric Chemistry and Physics*, 17(11), 7055–7066.
- Plumb, R. A., & Ko, M. K. (1992). Interrelationships between mixing ratios of long-lived stratospheric constituents. *Journal of Geophysical Research: Atmospheres*, 97(D9), 10145–10156.
- Randel, W. J., Park, M., Emmons, L., Kinnison, D., Bernath, P., Walker, K. A., . . . Pumphrey, H. (2010). Asian monsoon transport of pollution to the stratosphere. *Science*, 328(5978), 611–613.
- Schwantes, R. H., Lacey, F. G., Tilmes, S., Emmons, L. K., Lauritzen, P. H., Walters, S., . . . others (2022). Evaluating the impact of chemical complexity and horizontal resolution on tropospheric ozone over the conterminous us with a global variable resolution chemistry model. *Journal of Advances in Modeling Earth Systems*, 14(6), e2021MS002889.
- Strahan, S., Duncan, B., & Hoor, P. (2007). Observationally derived transport diagnostics for the lowermost stratosphere and their application to the gmi chemistry and transport model. *Atmospheric Chemistry and Physics*, 7(9), 2435–2445.
- Tang, W., Emmons, L. K., Worden, H. M., Kumar, R., He, C., Gaubert, B., . . . others (2023). Application of the multi-scale infrastructure for chemistry and aerosols version 0 (musicav0) for air quality in africa. *Geoscientific Model Development Discussions*, 2023, 1–34.
- Toon, O. B., Maring, H., Dibb, J., Ferrare, R., Jacob, D. J., Jensen, E. J., . . . others (2016). Planning, implementation, and scientific goals of the studies of emissions and atmospheric composition, clouds and climate coupling by regional surveys (seac4rs) field mission. *Journal of Geophysical Research: Atmospheres*, 121(9), 4967–5009.
- Ulanovsky, A., Yushkov, V., Sitnikov, N., & Ravengnani, F. (2001). The fozan-ii fast-response chemiluminescent airborne ozone analyzer. *Instruments and Experimental Techniques*, 44, 249–256.
- Viciani, S., Montori, A., Chiarugi, A., & D’Amato, F. (2018). A portable quantum cascade laser spectrometer for atmospheric measurements of carbon monoxide. *Sensors*, 18(7), 2380.
- Villamayor, J., Iglesias-Suarez, F., Cuevas, C. A., Fernandez, R. P., Li, Q., Abalos, M., . . . others (2023). Very short-lived halogens amplify ozone depletion trends in the tropical lower stratosphere. *Nature Climate Change*, 1–7.
- Vogel, B., Günther, G., Müller, R., Groöß, J.-U., & Riese, M. (2015). Impact of different asian source regions on the composition of the asian monsoon anticy-

- 776 clone and of the extratropical lowermost stratosphere. *Atmospheric chemistry*
777 *and physics*, 15(23), 13699–13716.
- 778 Vogel, B., Müller, R., Günther, G., Spang, R., Hanumanthu, S., Li, D., ... Stiller,
779 G. P. (2019). Lagrangian simulations of the transport of young air masses to
780 the top of the asian monsoon anticyclone and into the tropical pipe. *Atmo-*
781 *spheric Chemistry and Physics*, 19(9), 6007–6034.
- 782 von Hobe, M., Ploeger, F., Konopka, P., Kloss, C., Ulanowski, A., Yushkov, V.,
783 ... others (2021). Upward transport into and within the asian monsoon
784 anticyclone as inferred from stratoclim trace gas observations. *Atmospheric*
785 *Chemistry and Physics*, 21(2), 1267–1285.
- 786 Yan, X., Konopka, P., Ploeger, F., Podglajen, A., Wright, J. S., Müller, R., & Riese,
787 M. (2019). The efficiency of transport into the stratosphere via the asian and
788 north american summer monsoon circulations. *Atmospheric Chemistry and*
789 *Physics*, 19(24), 15629–15649.
- 790 Yin, M. T. (1949). Synoptic-aerologic study of the onset of the summer monsoon
791 over india and burma. *Journal of Atmospheric Sciences*, 6(6), 393–400.
- 792 Yushkov, V., Oulanovsky, A., Lechenuk, N., Roudakov, I., Arshinov, K., Tikhonov,
793 F., ... Georgiadis, T. (1999). A chemiluminescent analyzer for stratospheric
794 measurements of the ozone concentration (fozan). *Journal of Atmospheric and*
795 *Oceanic Technology*, 16(10), 1345–1350.
- 796 Zhang, G., & McFarlane, N. (1995). Sensitivity of climate simulations to the pa-
797 rameterization of cumulus convection in the canadian climate centre general
798 circulation model. *Atmosphere Ocean*, 33, 407–446.